

Flocking in One Dimension: Asters and Reversals

Brieuc Benvegnen,¹ Hugues Chaté,^{2,3,1} Pavel Krapivsky,⁴ Julien Tailleur,⁵ and Alexandre Solon¹

¹*Sorbonne Université, CNRS, Laboratoire de Physique Théorique de la Matière Condensée, 75005 Paris, France*

²*Service de Physique de l'Etat Condensé, CEA, CNRS Université Paris-Saclay, CEA-Saclay, 91191 Gif-sur-Yvette, France*

³*Computational Science Research Center, Beijing 100094, China*

⁴*Department of Physics, Boston University, Boston, MA 02215, USA*

⁵*Université Paris Cité, Laboratoire Matière et Systèmes Complexes (MSC), UMR 7057 CNRS, F-75205 Paris, France*

(Dated: September 15, 2022)

We study the one-dimensional active Ising model in which aligning particles undergo diffusion biased by the signs of their spins. The phase diagram obtained varying the density of particles, their hopping rate and the temperature controlling the alignment shows a homogeneous disordered phase but no homogeneous ordered one, as well as two phases with localized dense structures. In the flocking phase, large ordered aggregates move ballistically and stochastically reverse their direction of motion. In what we termed the “aster” phase, dense immobile aggregates of opposite magnetization face each other, exchanging particles, without any net motion of the aggregates. Using a combination of numerical simulations and mean-field theory, we study the evolution of the shapes of the flocks, the statistics of their reversal times, and their coarsening dynamics. Solving exactly for the zero-temperature dynamics of an aster allows us to understand their coarsening, which shows extremal dynamics, while mean-field equations account for their shape.

CONTENTS

I. INTRODUCTION

I. Introduction	1
II. Model and its phases	2
A. 1D active Ising model	2
B. The three phases	3
C. Fate of the liquid-gas transition scenario	3
III. The flocks and their reversals	4
A. The shape of a flock	4
B. Statistics of reversal times	6
C. Role of the parameters D , ε and β	8
D. Coarsening	9
IV. Asters	10
A. Lifetime of an aster at zero temperature	10
B. Coarsening at small temperature	12
C. Shape of asters	13
V. Conclusion	14
Acknowledgments	15
A. Numerical simulations	15
1. Discrete-time simulations	15
2. Continuous-time simulations	15
3. Numerical procedure to spatially align flocks.	16
B. Another zero-temperature limit	16
References	17

Active matter often consists of large assemblies of self-propelled particles. The variety of collective behaviors that they exhibit has come under intense scrutiny [1–4]. This interest stems from both the pervasiveness of active matter in nature, from molecular motors [5, 6] to bacterial swarms [7–11] and animal groups [12–15], and from the possibility to synthesize various kinds of self-propelled particles, such as chemically propelled Janus particles [16–19], rolling colloids [20–23] or vibrated macroscopic objects [24–26].

A challenge for physicists is to understand the fundamental differences between active matter, on the one hand, and passive systems or other classes of nonequilibrium systems, on the other hand. The role of fluctuations offers a striking example of such differences. Indeed, following the introduction of the Vicsek model [27], it was realized by Toner and Tu [28] that self-propelled particles with a local ferromagnetic alignment of their direction of motion, a “flying XY model”, exhibit an ordered phase of collective motion even in two-dimensions (2D), whereas such a phase would be destroyed by fluctuations in a passive system, as requested by the Mermin-Wagner theorem [29]. Although they do not destroy the ordered state, density fluctuations are measured to be anomalously large [30–33]. The nature of the transition to the ordered state of collective motion from a disordered system shows another role of fluctuations. At mean-field level the transition is predicted to be continuous for many systems [34–37] but becomes discontinuous once fluctuations are accounted for [38]. This translates into large finite-size effects in simulations: The transition seems continuous in small systems [27] but appears discontinuous [31, 39], akin to a liquid-gas transition, for large-enough system sizes [37, 38, 40].

The effect of fluctuations is most prominent in 1D.

For a passive system with short-range interactions, the Van Hove theorem forbids a phase transition at non-zero temperature in absence of long-ranged interactions [41]. Nonequilibrium systems can evade this requirement: For example driven diffusive systems show boundary-induced phase transitions [42–44]. One-dimensional active systems also order and they do so in a peculiar way. It was shown in several models of aligning self-propelled particles that when the noise on alignment is reduced, the system transitions from a disordered state to a state where a finite fraction of all particles is contained in a single ordered aggregate [37, 45–50]. This “flock” progressively spreads while propagating ballistically until it spontaneously reverses its direction of motion under the action of fluctuations. Because the time between two reversals increases only logarithmically with system size [46], there is no symmetry breaking asymptotically [37]. The situation is that of a stochastically switching global order, even in infinite systems.

One-dimensional flocking is also relevant experimentally. Locusts marching in a quasi-1D ring-shaped arena order if they are sufficiently dense and show spontaneous reversals of the global direction of motion [51, 52]. Recently, the collective motion of cells confined to 1D race-tracks has also been studied in detail [53].

Here, we analyze the 1D version of the active Ising model (AIM), first introduced in Ref. [37]. This lattice model only involves ferromagnetic alignment and self-propulsion, with no excluded volume or other interaction. We explore the phase diagram in terms of the temperature controlling the aligning interaction, the hopping rate, and the average density of particles. Consistently with previous studies considering different implementations of the same ingredients [45, 46, 48–50], we observe a transition from a disordered state to a flocking state featuring a single moving aggregate, which stochastically reverses its direction of motion. Although this transition was reported to be continuous in early papers on related 1D models [45, 46], it was found to be discontinuous in Ref. [37], a fact that is somewhat hidden by reversals. Here we clarify the connection with the liquid-gas transition happening in 2D [37, 54] by showing that the flocks tend to relax to a phase-separated state but are prevented to do so by reversals. Moreover, we confirm the logarithmic scaling with system size of the average reversal time found in Ref. [46] for a different 1D flocking model and track down its origin. At low temperature and/or hopping rate, when alignment dominates over self-propulsion, we encounter a different type of structure that we term “asters”. These asters are static structures composed of two highly localized peaks of opposite magnetization that exchange particles back and forth. We first account for the remarkable stability of these structures by solving exactly the dynamics of a single aster at zero temperature (this is the asymptotic configuration then). We then discuss the finite-temperature coarsening of asters and show the existence of two possible scenarios leading either to macroscopic condensation or to an ex-

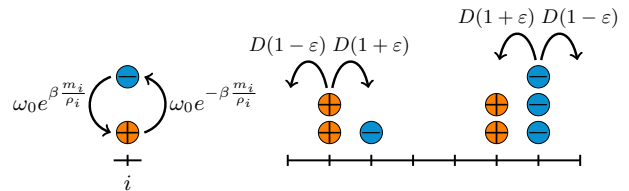


FIG. 1. Sketch of the two possible actions, spin-flipping and hopping, and their associated rates.

tensive number of asters possessing a characteristic size. Finally, we derive the steady-state profile of the asters in the mean-field approximation, which turns out to be very accurate.

This article is organized as follows: In Sec. II we first define the AIM and present the three phases observed in our simulations (disordered, flocking and aster phases) with phase diagrams for the main parameters of the model. We then investigate the two non-trivial phases. In Sec. III, we successively look at the shapes of asters and how they evolve in time (Sec. III A), the statistics of reversals (Sec. III B), and the two distinct regimes observed at small and large velocity and/or temperature (Sec. III C). We then investigate the aster phase in Sec. IV. We first derive an exact solution for the dynamics of an aster at zero temperature in Sec. IV A, before looking at the coarsening dynamics at small-but-finite temperature in Sec. IV B and investigating the aster shape in Sec. IV C.

II. MODEL AND ITS PHASES

A. 1D active Ising model

Following Refs. [37, 54], we consider N particles on a ring of L sites. There is no excluded-volume interaction so that each site can accommodate an arbitrary number of particles. Each particle carries an Ising spin $s = \pm 1$ and undergoes biased diffusion: A particle with spin s hops to the next site on its right (resp. left) at rate $D(1 + s\epsilon)$ (resp. $D(1 - s\epsilon)$). The parameter $\epsilon \in [0, 1]$ controls the asymmetry between the passive limit $\epsilon = 0$ and the fully asymmetric hopping $\epsilon = 1$, while D controls the overall hopping frequency. In average, a particle thus moves at a speed $v = 2D\epsilon a$ in the direction set by the sign of its spin, a being the lattice spacing. Finally, on a site i occupied by n_i^+ and n_i^- particles with spins $+1$ and -1 , respectively, a particle of spin s flips at a rate

$$W(s \rightarrow -s) = \omega_0 e^{-\beta s \frac{m_i}{\rho_i}}, \quad (1)$$

where $\rho_i = n_i^+ + n_i^-$ and $m_i = n_i^+ - n_i^-$ are the local density and magnetization. This rate is chosen such that the flipping dynamics of each site i is independent and corresponds to that of a fully-connected on-site Ising model with Hamiltonian $-m_i^2/(2\rho_i)$ undergoing an equilibrium dynamics at inverse temperature $\beta = 1/T$. The

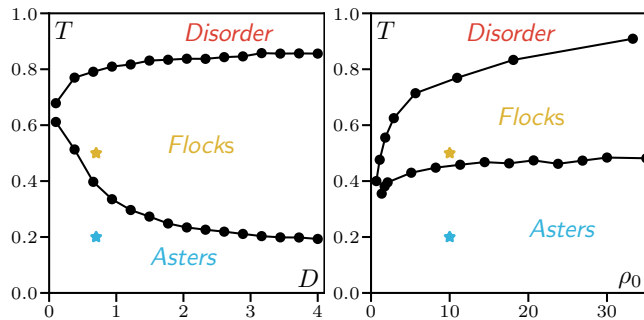


FIG. 2. Phase diagrams in the (hopping-rate, temperature) plane at $\rho_0 = 10$ and $\varepsilon = 0.7$ (left) and (density, temperature) plane at $D = 0.5$ and $\varepsilon = 0.7$ (right). The stars indicate the parameters used in Fig. 3 to illustrate the phases. The line separating the disordered and flocking phases in the (ρ_0, T) plane is set by the density $\rho_g(T)$ of the gas in the flocking states at temperature T (see Sec. II C). The other lines are determined using the threshold $\langle |\tilde{m}| \rangle = 0.05$ on the time-averaged magnetization per particle, which is non-zero only in the flocking phase. Data obtained in a system of size $L = 500$; increasing system size displaces the lines only within the size of the symbols.

two actions (hopping and flipping spin) and the associated rates are depicted in Fig. 1. Note that the model is out of equilibrium even at $\varepsilon = 0$ since the symmetric hopping dynamics is insensitive to the changes of the total Hamiltonian $H = -\sum_i m_i^2/(2\rho_i)$ [55].

In the rest of the paper, we choose without loss of generality $\omega_0 = a = 1$ thus fixing the time and space units. We study the system as a function of the parameters β (or T), D , ε and the average density $\rho_0 = N/L$. Our simulations relied either on discrete time steps with random sequential updates or on an exact continuous-time Monte Carlo algorithm. The efficiencies of both schemes depend on the temperature and phases under study, as detailed in Appendix A.

B. The three phases

Looking at the phase diagrams in the $D-T$ and ρ_0-T planes shown in Fig. 2 (and in the qualitatively similar $\varepsilon-T$ diagram not shown), we see that, as expected, the system is disordered at high temperature. Density and magnetization are homogeneous and fluctuate, respectively, around ρ_0 and 0.

Decreasing temperature, the system reaches a flocking phase which consists, at long times, of a single dense ordered aggregate moving ballistically in a disordered gas, as illustrated on the snapshot shown in Fig. 3c. These “flocks” have a rather complex dynamics: They slowly but regularly widen as they travel, and undergo stochastic reversals during which they “regroup” into a very thin condensate and their magnetization changes sign. These dynamics, together with the coarsening leading to a single aggregate, are displayed in the space-time diagram of

Fig. 3e, and form the topic of Sec. III. Note that transient, finite-size aggregates can be observed to move ballistically in the gas region surrounding the main aggregate (see Fig. 3e).

Finally, at lower temperatures, the system exhibits what we have called asters, that are illustrated in the snapshot shown in Fig. 3d: Sharp peaks of positive and negative magnetizations, spread over a few sites, face each other. These structures are long-lived, despite the absence of repulsive interactions. As shown on the space-time plot Fig. 3f, asters can dissolve on long time scales, leading to coarsening. Our study of this phase is in Sec. IV.

To distinguish between the three phases, we introduce two order parameters, the magnetization per particle $\tilde{m} = \sum_{i=1}^N s_i/N$, which is non-zero at long times only in the flocking phase where it alternates between a positive and a negative value because of reversals, and the fraction ϕ of particles contained in asters. Our criterion to detect an aster is to find two adjacent sites with magnetization of opposite sign and density larger than $2\rho_0$. (This value is chosen such that asters are robustly detected while not erroneously counting fluctuations as asters. Our results do not depend on the precise criterion used.) The two order parameters are shown as a function of time in the flocking and aster phases (Fig. 3a-b).

C. Fate of the liquid-gas transition scenario

In 2D, the transition to collective motion in polar flocking models has been shown to be akin to a liquid-gas transition between a disordered gas and a polar ordered liquid [37, 54]. The form of the phase coexistence depends on the symmetry of the spins: for the Vicsek model with continuous spins one observes microphase separation with an extensive number of dense ordered traveling bands having a characteristic size, while in the AIM, which has a discrete spin symmetry, one obtains phase separation between two macroscopic domains [40].

In the same way, in 1D one observes the coexistence of an ordered flock with a disordered gas. Although, because of fluctuations it can easily be mistaken for a continuous transition [45, 46], the transition between the disordered phase and the flocking state also shows a phase-separation scenario. In particular, the transition exhibits metastability and the telltale negative peaks in the Binder fourth-order cumulant for large (but finite) systems which arise from discontinuous nucleation events [37, 56]. In addition, the density in the gas is independent of the average density ρ_0 in the system.

However, looking at the phase diagram in the (ρ_0, T) plane (Fig. 2, right), a second transition line to a homogeneous ordered liquid is conspicuously absent. This is because, contrary to what happens in 2D, fluctuations destroy the homogeneous ordered phase in 1D. Indeed, as in Ref. [47], we see that, if we prepare the system in this state, it is metastable but eventually gets destabilized

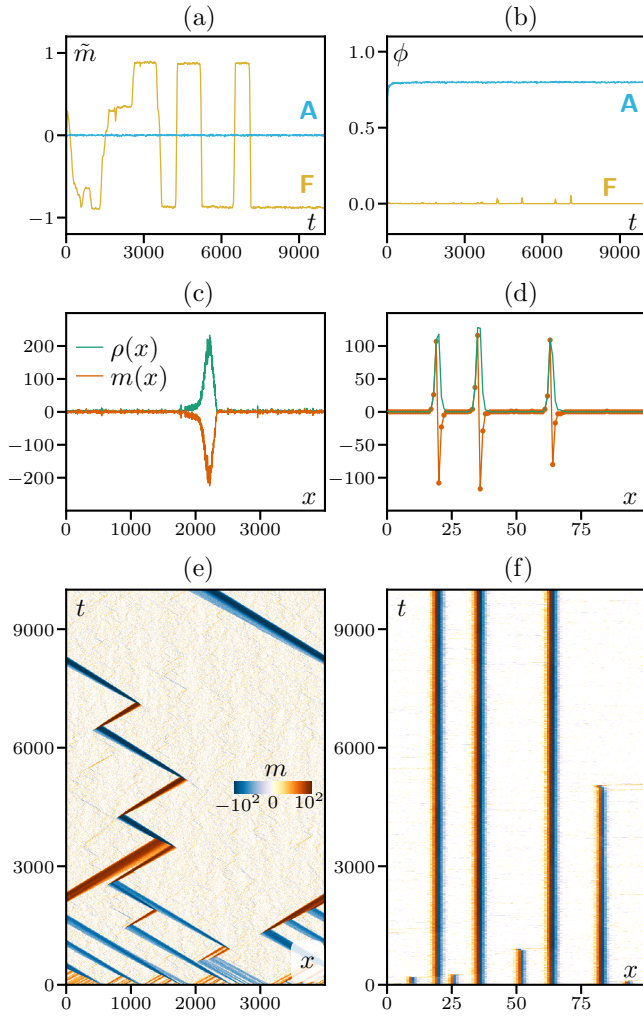
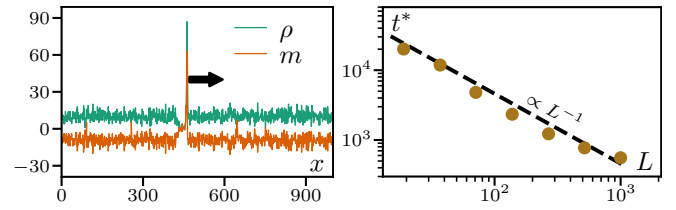


FIG. 3. **(a):** The magnetization per spin \tilde{m} , is non-vanishing only in the flocking phase. **(b):** The fraction of particles ϕ contained in asters is non-vanishing only in the aster phase. **(c-d):** Instantaneous density and magnetization fields at the final time $t = 10^4$ of the space-time diagrams shown in (e-f). **(e-f):** Space-time diagrams in the flocking (e) and aster (f) phases. The parameters, indicated by stars in the phase diagrams of Fig. 2, are $\rho_0 = 10$, $\varepsilon = 0.7$, $D = 0.5$ and $\beta = 2, 5$ for the F and A phases, respectively. The system sizes $L = 4000$ (F phase) and $L = 100$ (A phase) were chosen for legibility. Simulations are started from a homogeneous disordered initial condition. The runs in (a,b) for the A and F phases are the same as in (e,f).

by a fluctuation. As shown in the left panel of Fig. 4 (see also Supplementary Movie 1), a local fluctuation of the opposite magnetization propagates through the entire system, until only a localized flock remains. Thus, even if the probability of such a fluctuation may be rare, it increases linearly with system size since it can happen anywhere in the system. Therefore, we expect that the lifetime of the ordered phase decreases as L^{-1} , which is what we measure (see Fig. 4, right). At large enough



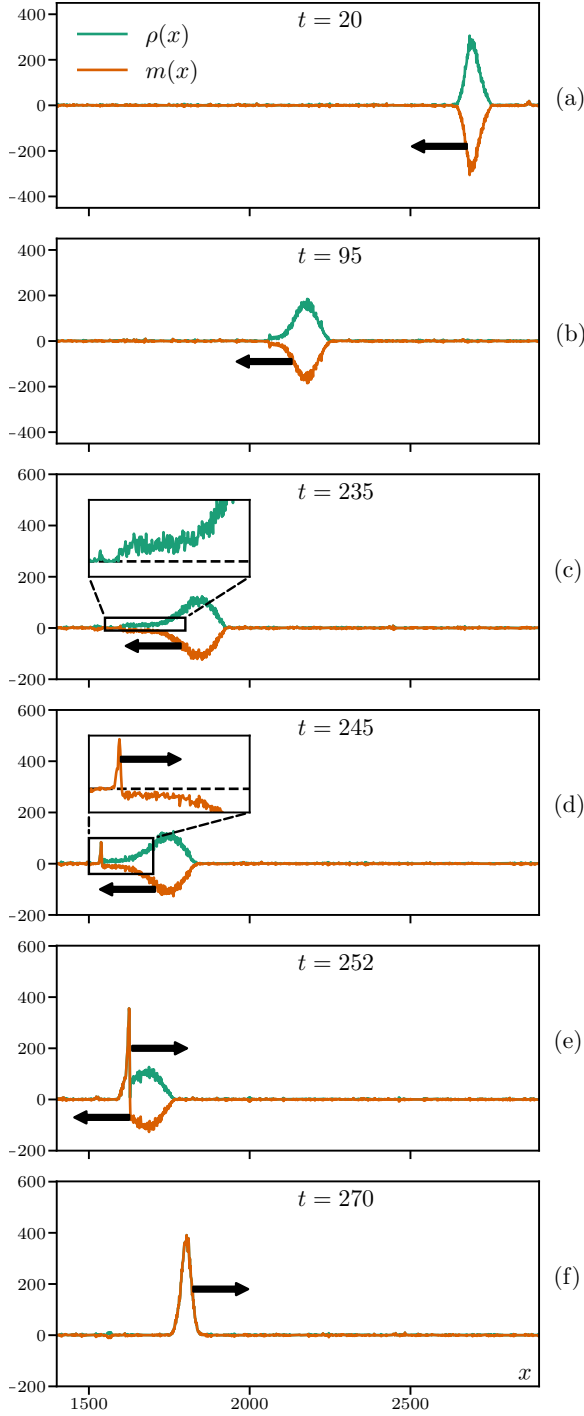


FIG. 5. Instantaneous density (green) and magnetization (orange) profiles during the spreading and the reversal of a flock. An initially peaked aggregate (a) spreads while propagating (b). After some time, it develops a protrusion at the leading edge (c). A spontaneous fluctuation at the front (d) can propagate inside the flock and progressively flip all the particle orientations (e). Finally, just after the reversal, one is left with a flock with the same shape as in (a) (which was taken just after the previous reversal), albeit with a reversed magnetization. Time is counted from the previous reversal. Parameters: $L = 4000$, $\beta = 2$, $\varepsilon = 1$, $D = 0.5$, $\rho_0 = 10$.

age t . As shown in Fig. 3a, the magnetization per spin \tilde{m} flips from a well defined value \tilde{m}_0 to $-\tilde{m}_0$ during a reversal. We define the time origin of each reversal as the time when $\tilde{m}(t) = -0.7\tilde{m}_0$. (The 0.7 factor works well, but other values are of course possible.) Flocks of the same age are localized at different positions on the lattice. A simple idea to align them so as to be able to average their shape would be to align their densest sites to try and match their peaks. However, this is very noisy and leads to large fluctuations that artificially smear out the flock shapes. Instead, we use the rear edges of the flocks, which are always very sharp. (The detailed aligning procedure is described in Appendix A 3.) This leads to satisfying results: As shown in Fig. 6a, flocks superimpose with little spread along most of their profiles, allowing to extract meaningful average shapes. Note however that the precise position of the leading edge fluctuates, leading to an average profile whose leading edge is smoother than that of the instantaneous ones. This confirms clearly the two features mentioned earlier: the flock contains a main peak which spreads continuously and, after some time, a protrusion with constant density and magnetization which develops at its leading edge (see Fig. 6b). We now discuss both of these features.

As shown in Fig. 6c, the main peak of the flock at a given age is proportional to the system size and contains a macroscopic fraction of the particles. The top of the peak is well approximated by a Gaussian with a variance σ^2 that is independent of system size and grows linearly in time (Fig. 6d). In addition, the peak propagates at a constant speed v_p , defined as the speed of the maximum of the density profile, which is smaller than the speed v of individual particles (Fig. 6e).

Since the peak contains a high density of particles, we expect it to be well described by a mean-field theory that we now construct starting from the microscopic dynamics, following Ref. [54]. To do so, we first write exact equations for the average density and magnetization $\langle \rho_i \rangle$ and $\langle m_i \rangle$ on site i , the average being over realizations of the stochastic microscopic dynamics. This gives

$$\partial_t \langle \rho_i \rangle = D \langle \rho_{i+1} + \rho_{i-1} - 2\rho_i \rangle - \frac{v}{2} \langle m_{i+1} - m_{i-1} \rangle \quad (2)$$

$$\partial_t \langle m_i \rangle = D \langle m_{i+1} + m_{i-1} - 2m_i \rangle - \frac{v}{2} \langle \rho_{i+1} - \rho_{i-1} \rangle + 2 \left\langle \rho_i \sinh \left[\beta \frac{m_i}{\rho_i} \right] - m_i \cosh \left[\beta \frac{m_i}{\rho_i} \right] \right\rangle \quad (3)$$

These equations are not closed since Eq. (3) involves the average of a nonlinear term. However, in the mean-field approximation where fluctuations and correlations are neglected, $\langle f(x) \rangle = f(\langle x \rangle)$ for any function f . Taking in addition the continuous limit, Eqs. (2)-(3) rewrite

$$\partial_t \rho = D \partial_x^2 \rho - v \partial_x m \quad (4)$$

$$\partial_t m = D \partial_x^2 m - v \partial_x \rho - 2m \cosh \left[\beta \frac{m}{\rho} \right] + 2\rho \sinh \left[\beta \frac{m}{\rho} \right]. \quad (5)$$

with $\rho(x = ia) = \langle \rho_i \rangle$ and similarly for m .

Contrary to the density field, $m(x, t)$ is a fast mode which relaxes rapidly to a value that makes the right-

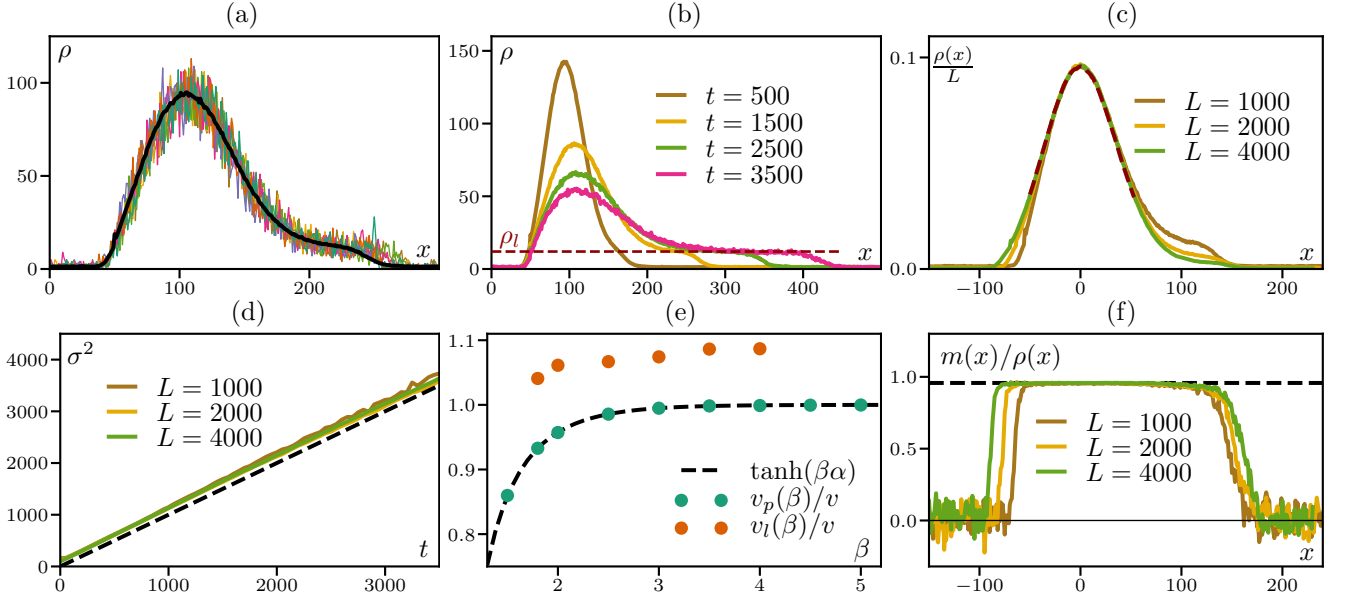


FIG. 6. **(a)**: Seven representative instantaneous density profiles (colors) superimposed to the average profile (thick black line). **(b)**: Evolution of the averaged density profile as a function of time. The red dashed line is a fit to the density ρ_ℓ of the protrusion. **(c)**: Average density profiles at $t = 1200$ showing that the main peak is extensive in system size. The red dashed line is a Gaussian fit used to compute the variance σ^2 in (d). **(d)**: Variance of the main peak. The dashed line is the mean-field prediction $\sigma^2 = 2Dt$. **(e)**: Speeds v_p of the main peak (computed as the speed of the maximum) and v_ℓ of the protrusion (computed as the speed of the point at $\rho = \rho_\ell/2$ in the average profiles) divided by the self-propulsion speed $v = 2D\varepsilon$. The dashed line is the mean-field prediction. **(f)**: Average polarization profile $m(x)/\rho(x)$. The dashed line is the mean-field prediction, solution of $m/\rho = \tanh(\beta m/\rho)$. Parameters: $\rho_0 = 10$, $\beta = 2$, $\varepsilon = 1$, $D = 0.5$, $t = 1000$ (a,c,e,f), $L = 1000$ (a,b), $L = 5000$ (e).

hand-side of Eq. (5) vanish. To leading order in a gradient expansion, this amounts to requiring that the interaction term in Eq. (5) vanishes, i.e. that $m/\rho = \tanh(\beta m/\rho)$. This thus predicts $\alpha = m/\rho$ to be the solution of $\alpha = \tanh(\beta\alpha)$, which is verified numerically in Fig. 6f. Using $m(x) = \alpha\rho(x)$ in Eq. (4), we obtain a diffusion-drift approximation for the density field:

$$\partial_t \rho = D \partial_x^2 \rho - v \tanh(\beta\alpha) \partial_x \rho. \quad (6)$$

The diffusion and drift coefficients read from Eq. (6) both match numerical measurements as seen in Fig. 6d-e.

Let us now turn to the protrusion appearing at the front of the flock. Since reversals start at the leading edge, this protrusion is expected to play an important role in the dynamics. Contrary to the main peak, it has a fixed height (in density and magnetization) independent of time and system size (not shown). Its velocity results both from the persistent hop of the particles and from the recruitment of new sites at the leading edge due to the aligning dynamics. This explains why the leading edge of the protrusion grows with a speed larger than the individual particle speed v (Fig. 6e), much like for the polar bands of the coexistence region in 2D [54]. The front speed is thus also larger than the drift velocity of the peak, which explains the increase of the protrusion length as time passes. All this suggests that the flock is trying to relax to the fixed density ρ_ℓ of the homogeneous

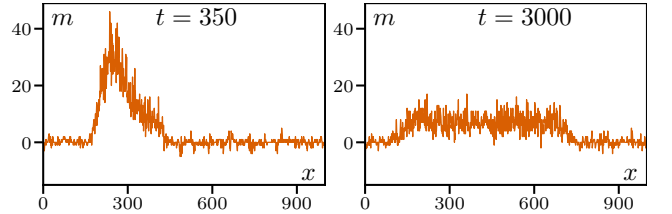


FIG. 7. Instantaneous density profile at times $t = 350$ (left) and $t = 3000$ (right) after the last reversal. The profile relaxes to a long-lived phase-separated state, whose shape is stationary (until the next reversal occurs). Parameters: $\rho_0 = 5$, $L = 1000$, $\beta = 2$, $\varepsilon = 1$ and $D = 2$.

ordered liquid but is prevented to do so by the reversals. This is confirmed by choosing parameters such that the full phase separation can be observed before a reversal happens. This is achieved in Fig. 7 by increasing D ; one then observes a relatively long-lived phase-separated profile.

B. Statistics of reversal times

The average time between two reversals, $\langle \tau \rangle$, shows a logarithmic increase with system size $\langle \tau \rangle \propto \log(L)$ (Fig. 8a). This is in line with previous results obtained

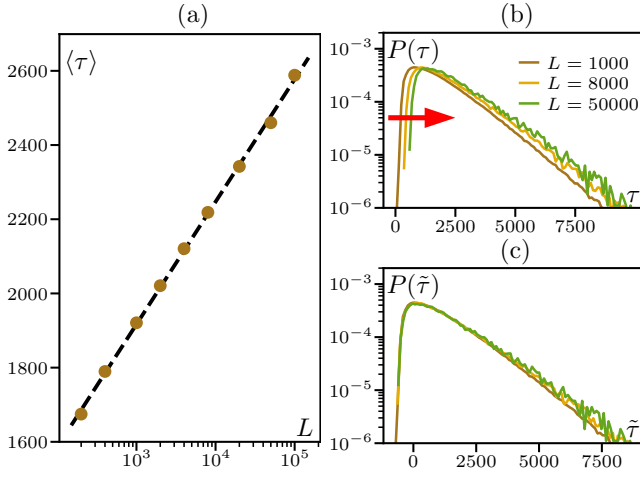


FIG. 8. **(a):** Mean time between reversals with a fit to a logarithmic function $f(L) = a \log L + b$, leading to $a = 139$ and $b = 964$ (dashed line). **(b):** Probability density function of the reversal time τ . The red arrow emphasizes the shift of the distributions at small τ responsible for the logarithmic scaling of the mean. **(c):** Same as in (b) with an horizontal shift $\tilde{\tau} = \tau - \alpha \log L$ with $\alpha = 110$. Parameters: $\rho_0 = 10$, $\beta = 2$, $\varepsilon = 1$, $D = 0.5$.

by O’Loan and Evans for a different model [46] (see also [47]), and it confirms that no true symmetry-breaking arises: the system spends finite fractions of time going to the right, to the left, and in the reversals [37].

To understand the physical origin of this logarithmic scaling, we consider $P(\tau)$, the distribution of inter-reversal times.

As shown in Fig. 8b, it has a peak and an approximately exponential tail with a decay rate that is roughly independent of L . Increasing L , the distribution shifts slightly to the right. As shown in Fig. 8c, a horizontal shift by $\alpha \log L$, with α a constant, collapses reasonably well the distributions obtained for several values of L .

To better characterize the various processes at play, we compute the reversal rate $\lambda(t)$, defined via the probability $\lambda(t)dt$ that a flock of age t reverses within $[t, t+dt]$. This rate is related to the distribution $P(\tau)$ via the number of flocks $N_f(t)$ that have survived until time t from an initial population of $N_f(0)$: $\dot{N}_f(t) = -\lambda(t)N_f(t)$ so that $\lambda = -\dot{N}_f/N_f$. In addition N_f itself is related to P through $N_f(t)/N_f(0) = \int_t^\infty P(\tau)d\tau$, which yields

$$\lambda(t) = \frac{P(t)}{\int_t^\infty P(\tau)d\tau}. \quad (7)$$

In physical terms, Eq. (7) simply states that the probability that an event happens at time t is the rate of occurrence of this event at time t multiplied by the probability that it did not happen before: $P(t) = \lambda(t)[1 - \int_0^t P(\tau)d\tau]$. Note that for an exponential distribution, λ equals the decay rate of the exponential. In Fig. 9a, we show $\lambda(t)$ computed using Eq. (7) for several system sizes. We see an initial rapid increase in λ , with a char-

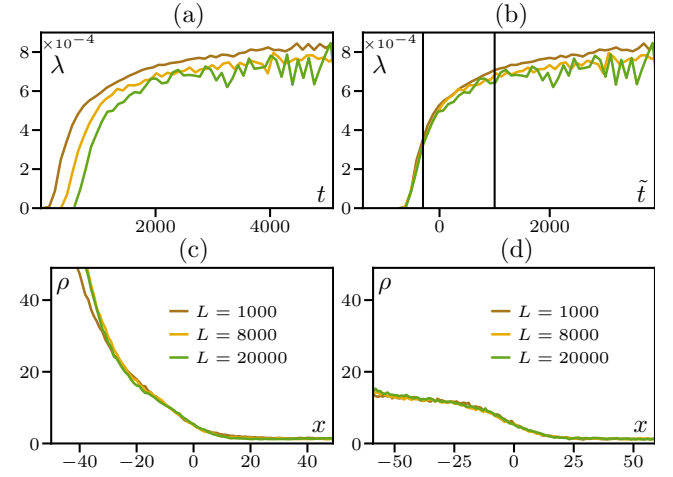


FIG. 9. **Top:** Rate of reversal $\lambda(t)$ as a function of time since the last reversal **(a)** and with time shifted as $\tilde{t} = t - \alpha \log L$ **(b)**, $\alpha = 110$ as in Fig. 8. **Bottom:** Average profiles at fixed \tilde{t} , at $\tilde{t} = -300$ when the protrusion just begins to appear **(c)**, and at $\tilde{t} = 1000$ when it has developed **(d)**. The corresponding times are indicated by vertical lines in panel (b). The profiles are aligned on the point where $\rho = 5$. Parameters: $\rho_0 = 10$, $\beta = 2$, $\varepsilon = 1$, $D = 0.5$.

acteristic time that increases with system size, followed by an approximately flat plateau corresponding to the exponential tail of $P(\tau)$. As shown in Fig. 9b, shifting the time by $\alpha \log L$ provides a good collapse of the curves $\lambda(t - \alpha \log L)$ measured for different system sizes, consistent with what was reported for $P(\tau - \alpha \log L)$ in Fig. 8.

The evolution of $\lambda(t)$ can be related to that of the shape of the flock. Reversals are initiated at the leading edge of flocks. At short times, the leading edge is very stiff so that there is little chance that a spontaneous fluctuation in the gas ahead, whose typical density is very low, triggers a reversal (Fig. 5a). Correspondingly, $\lambda(\tau) \rightarrow 0$ as $\tau \rightarrow 0$. At longer times two processes take place that make reversals more likely. First, flocks spread diffusively, due to the stochastic hopping of the particles. As the leading edge smoothens, it becomes more and more susceptible to fluctuations. Then, once the leading edge has sufficiently spread, its shape becomes compatible with the development of a liquid phase [57]. As this liquid protrusion develops, the shape of its leading front becomes constant in time (Fig. 5b). The probability that a fluctuation flips the protrusion becomes time-independent, leading to a plateau value of $\lambda(t)$ at late times, independent of L .

Let us now try to rationalize the scaling form $P(\tau - \alpha \log L)$ and $\lambda(t - \alpha \log L)$ reported in Figs. 8 and 9. We see in Figs. 9c-d that the leading edges of the density profiles also collapse under the same shift. To account for this, we compute the time t^* it takes for the profile to reach a given slope $-k^*$ at a given density ρ_ℓ :

$$\rho(x, t^*) = \rho_\ell; \quad \partial_x \rho(x, t^*) = -k^*. \quad (8)$$

We first focus on the early-time dynamics, where we

expect a Gaussian spreading in the co-moving frame. There, the density profile can be approximated as

$$\rho(x, t) = \frac{N_0}{\sqrt{2\pi Dt}} e^{-\frac{x^2}{4Dt}}, \quad (9)$$

where D is an effective diffusion coefficient and $N_0 = L\rho_0$ is the number of particles in the aggregate. Denoting by x^* the position at which the density profile equals ρ_ℓ , we find that the slope satisfies $k^* = x^*\rho_\ell/(2Dt)$ while x^* is given by

$$x^* = 2\sqrt{Dt} \sqrt{\log \frac{N_0}{\rho_\ell} - \frac{1}{2} \log(2\pi Dt)}. \quad (10)$$

The slope as a function of time then satisfies

$$k(t) = \rho_\ell \sqrt{\frac{\log \frac{N_0}{\rho_\ell}}{Dt} \left(1 - \frac{1}{2} \frac{\log 2\pi Dt}{\log \frac{N_0}{\rho_\ell}} \right)}. \quad (11)$$

At early times and large system sizes, $\log(2\pi Dt) \ll \log \frac{N_0}{\rho_\ell} \propto \log L$, so that k is a function of $t/\log L$. Note that assuming a rate of reversals controlled by the slope of the front would lead to scaling forms $P(\tau/\log L)$ and $\lambda(t/\log L)$ during the early Gaussian spreading of the flock.

After a time t_{prot} that can be estimated as the inflexion point in Fig. 9a, the protrusion grows out of the main peak. Afterwards, the diffusive spreading of the main peak does not affect the leading edge anymore. At this stage, $\lambda(t)$ keeps increasing for some time, since the flipping of larger protrusions is more likely to generate a peak with a mass sufficient to revert the whole flock. In addition, $\lambda(t)$ also increases after t_{prot} because of the slight dispersal in flock shapes shown in Fig. 6: as the time since the last reversal increases, so does the fraction of flocks with a liquid protrusion. For $t > t_{\text{prot}}$, the $\tau/\log L$ scaling stops since the leading edge converges to a well-defined steady profile. The time t_{prot} can then be estimated by the time it takes for the front to reach the slope corresponding to the liquid protrusion, so that $t_{\text{prot}} \propto \log L$.

We thus expect two different scaling regimes: an initial Gaussian spreading leading to $\lambda(t/\log L)$ and a late-time scaling form $\lambda(t - \alpha \log L)$, once the protrusion has grown out of the main peak. As shown in Fig. 9c-d, the protrusion grows out quite early so that the first regime is never quantitatively observed in our simulations: most reversals take place after the protrusion has grown out. This explains why the $\lambda(t - \alpha \log L)$ and $P(\tau - \alpha \log L)$ scalings work satisfactorily.

C. Role of the parameters D , ε and β

Most results presented so far were obtained at fixed, rather typical, parameter values. We now report on the

effect of changing the three parameters D , ε and β . Figure 10 shows how $\langle \tau \rangle$ and λ , the reversal rate extracted from the exponential tail of $P(\tau)$, vary with each of these parameters, keeping the other two constant.

Comparing $\langle \tau \rangle$ with λ^{-1} (which is the mean of a normal exponential distribution with rate λ), we see that λ^{-1} ‘underestimates’ $\langle \tau \rangle$ but that both quantities essentially vary in the same manner. (Their difference is due to the transient regime before $\lambda(t)$ reaches its asymptotic value, as shown in Fig. 9a-b.) To account for the variations of $\langle \tau \rangle$, we can thus focus on the reversals at late times, which take place after the protrusion has developed at the front of the flocks.

We find that the divergences of $\langle \tau \rangle$ visible on Fig. 10 can be explained by two different mechanisms. First, decreasing D or ε or increasing β while keeping the other parameters fixed brings the system from the flocking phase to the aster phase (see the phase diagrams in Fig. 2). Close to the transition, transient asters appear at the beginning of an attempted reversal, as shown in Fig. 11e. Once the aster is formed, the propagation of the fluctuation stops until the aster dissolves. (See section Sec. IV for a detailed discussion on aster dynamics.) In the mean time, a large amount of particles arrive from the flock, which tends to destroy the aster and resume the forward motion of the flock. This process thus tends to suppress reversals: transient asters protect the flock against fluctuations, hence increasing their lifetime.

The other divergences of $\langle \tau \rangle$, in the large D and small β limits, can be accounted for by comparing the roles of diffusion and alignment during a reversal. Aligning interactions tend to flip particles from the flock, hence strengthening the fluctuation. On the contrary, diffusion damps the fluctuation as it propagates. Diffusion dominates when D/e^β —the ratio of hopping to alignment rates—increases, i.e. when D increases or β decreases. Figure 10 shows a steeper divergence when varying β compared to varying D , as expected from this reasoning.

To support these two scenarios, we now evaluate how likely a fluctuation is to reverse a flock in an idealized situation. We consider the deterministic mean-field evolution of an initial fluctuation of tunable size that encounters an ordered phase mimicking the protrusion of a flock at density ρ_ℓ and magnetization m_ℓ such that $m_\ell/\rho_\ell = \tanh(\beta m_\ell/\rho_\ell)$ (its mean-field value).

The initial condition is depicted in Fig. 11a and the evolution is that of Eqs. (2)-(3) after one takes a mean-field approximation for the nonlinear terms. We choose $\rho_\ell = 1$ without loss of generality, thus fixing the unit of density, and take the initial fluctuation to be fully ordered with magnetization $-\delta m$ and density δm , propagating to the left. We observe that there is a value δm^* such that small fluctuations $\delta m < \delta m^*$ do not propagate and the system remains ordered, whereas large fluctuations $\delta m > \delta m^*$ propagate and flip the entire initial flock [58]. This critical fluctuation size varies with the parameters, as shown in Fig. 11b where we vary D for several values of β . At small D we see the transient asters observed in

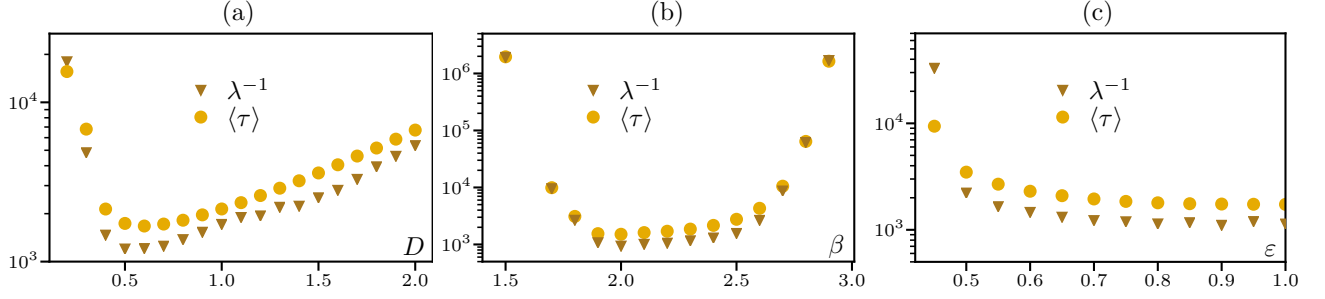


FIG. 10. Mean reversal time $\langle\tau\rangle$ as a function of D for $\beta = 1.8$ and $\varepsilon = 0.8$ (a), of β with $D = 0.5$ and $\varepsilon = 0.8$ (b), and of ε with $\beta = 2$ and $D = 0.5$ (c). The data are compared with the characteristic time λ^{-1} that corresponds to a purely exponential distribution $P_{\text{exp}}(\tau) = \lambda e^{-\lambda\tau}$, with λ measured from the tail of the true distribution $P(\tau)$. Parameters: $\rho_0 = 3$, $L = 1000$.

the microscopic model whereas they are not observed for larger D (see Fig. 11c-d). The variations of δm^* are consistent with the variations of $\langle\tau\rangle$ in the microscopic model as we see a sharp increase at small D corresponding to the appearance of transient asters and a slower increase at high D with no asters. This minimal model of reversals, despite its simplicity, thus reproduces the basic features of the mean reversal time and supports the two scenarios outlined above for the divergences of $\langle\tau\rangle$.

D. Coarsening

So far we only considered the steady-state regime where the system contains a single flock. We now study the coarsening dynamics that bring the system from a disordered initial condition to such a steady state. As shown on the space-time diagram of Fig. 3e, many small flocks form at early times and merge when they encounter until only one remains. The evolution of the number of flocks N_f can be written as

$$\dot{N}_f(t) = -\frac{N_f(t)}{t_{\text{coll}}(t)} \quad (12)$$

with a function $t_{\text{coll}}(t)$ that may depend on N_f and which we can interpret as the mean time before a flock collisions with a neighboring one.

We can anticipate two regimes for this collision time. At early times, when flocks are close to one another, they typically encounter a neighbouring flock before reversing their direction. The collision time will then be the ballistic time $t_{\text{coll}}^B = \ell/v$ with $\ell = L/N_f$ the mean distance between flocks. At later times, flocks are further apart and thus reverse their direction of motion before colliding. The collision time then has a diffusive scaling $t_{\text{coll}}^D = \ell^2/(2D_{\text{eff}})$ with the effective diffusion coefficient $D_{\text{eff}} = v^2\langle\tau\rangle$. The crossover between these two regimes is expected at a time t_c such that $t_{\text{coll}}^B(t_c) = \langle\tau\rangle$. Solving Eq. (12) in the ballistic regime gives

$$N_f(t) = \frac{L}{\frac{L}{N_f(0)} + vt} \quad (13)$$

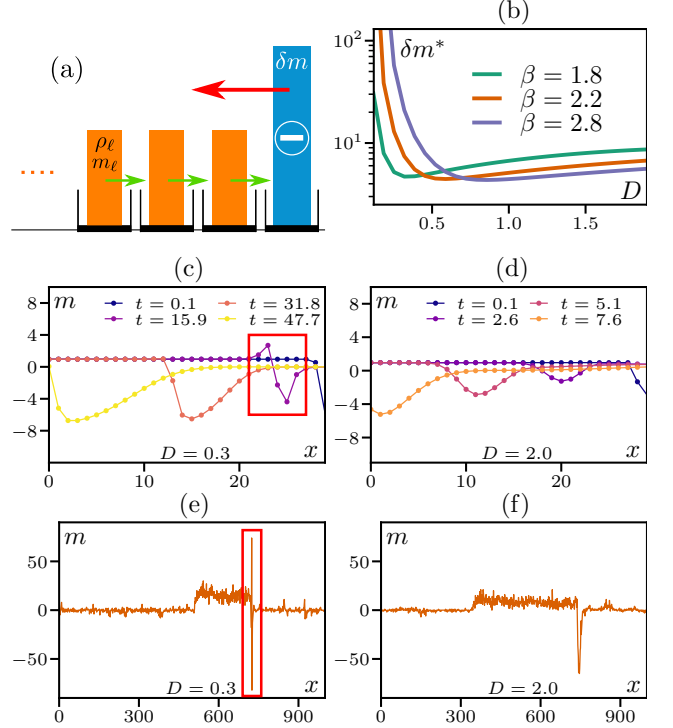


FIG. 11. (a): Sketch of the initial condition in the reduced mean-field model. (b): Minimal fluctuation δm^* necessary to reverse the flock in the reduced model. (c,d): Evolution of the density profile in the reduced model at low $D = 0.3$ (c) and high $D = 2.0$ (d) for fluctuations $\delta m = 8$ (c) and $\delta m = 6$ (d), slightly bigger than δm^* . Other parameters: $\varepsilon = 1$ and $\beta = 2$. (e,f) Instantaneous profiles in the microscopic model at the beginning of a reversal at low $D = 0.3$ (e) and high $D = 2$ (f). The transient aster (red boxes) observed at low D in the reduced model also appears in the full AIM. $\rho_0 = 5$, $L = 1000$, $\varepsilon = 1$ and $\beta = 2$.

from which we deduce that the crossover time is

$$t_c = \langle\tau\rangle - \frac{L}{vN_f(0)}. \quad (14)$$

Neglecting the dependence of $\langle\tau\rangle$ on $\log L$, which would give subdominant corrections, the number of flocks in

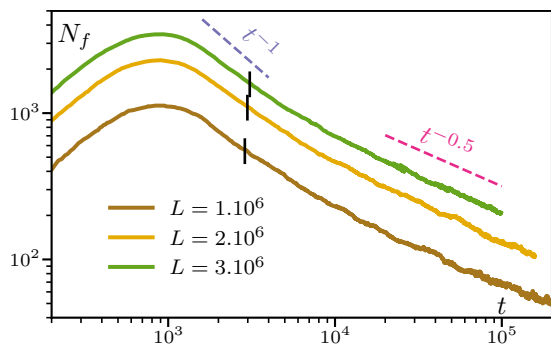


FIG. 12. Number of flocks N_f as a function of time, starting from a homogeneous disordered initial conditions. The short vertical black lines indicate the crossover time t_c as given in Eq. (14). $\rho_0 = 10$, $\beta = 2$, $D = 0.5$, $\varepsilon = 1$.

the diffusive regime then follows $\dot{N}_f \propto -N_f^3$ and thus $N_f(t) \sim 1/\sqrt{t}$.

Comparing with simulations in Fig. 12, we see that the late-time coarsening is indeed clearly diffusive. At short time, we first see an increase in the number of flocks corresponding to the time that they form and grow large enough to be detected by our algorithm (we use a system of two thresholds at $\rho = 2$ and $\rho = 8$ with spatial smoothing on the length $\delta x = 50$ to detect the flocks robustly). The crossover time t_c is then computed from Eq. (14), taking the initial time to be the time with the maximum number of flocks, and we indicate t_c by black lines in Fig. 12. Consistently with the analysis above, we do see a faster-than-diffusive coarsening in the short window before t_c .

IV. ASTERS

At low temperature or small velocity, a phase develops in which static structures coexist with a dilute gas. (See the phase diagrams in Fig. 2 and the snapshot in Fig. 3d.) Each of these ‘asters’ consists in two peaks of right and left-moving particles which apparently ‘block’ each other. Remember, however, that there is no exclusion in our model so that the underlying mechanism is necessarily more complex and calls for an explanation. We termed these structures asters, by analogy to the star-shaped defects observed in 2D active systems [59, 60].

A closer look at the microscopic dynamics of an aster reveals that its stability arises from periodic orbits in configuration space, as illustrated in Fig. 13. Starting from two peaks of opposite magnetization, one particle—say with positive spin—hops forward and lands onto the second site where it belongs to the minority phase. It then flips and aligns with its new environment. The most likely move is then that one of the minus particles hops forward onto the site populated by plus particles. Once again, this particle belongs to the minority phase and flips, leading the system back into its original state.

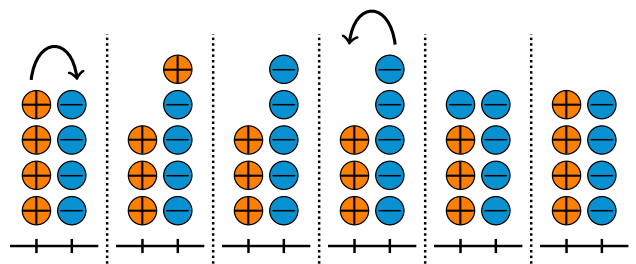


FIG. 13. A typical sequence of configurations that make asters stable at low temperature.

At low temperatures, such trajectories are much more likely than trajectories leading to the evaporation of the aster. To quantify the stability of asters, we first consider in Sec. IV A a zero-temperature fully-asymmetric model in which the lifetime of an aster can be computed exactly. We then discuss the stability of asters at finite temperature and the corresponding coarsening dynamics in Sec. IV B. Finally, we show in Sec. IV C that, for $0 < \varepsilon < 1$, asters typically have a richer shape than suggested by Fig. 13: they are not perfectly localized and admit an exponential tail with a characteristic size. Using a mean-field approximation, we compute the corresponding decay length and determine a necessary condition for the existence of asters that captures qualitatively, albeit not quantitatively, the phase boundary between flocks and asters shown in Fig 2.

A. Lifetime of an aster at zero temperature

To make progress analytically, we first consider a $T = 0$, fully asymmetric version of the AIM. Particles hop at rate $v = 2D$ and the aligning interaction is resolved instantaneously, due to the $\beta \rightarrow \infty$ limit of the flipping rate (1). In practice, when a particle hops onto a new site with two particles or more, it immediately acquires the magnetization of the target site. The limit is ill defined when one has both $m_i = 0$ and $\beta = \infty$. For simplicity, we here assume that when a particle of spin s arrives on a site occupied by a particle of spin $-s$, it flips and acquires a $-s$ spin. As a result, the sole microscopic time-scale of the system is v^{-1} . The case in which both particles keep their current spins and flip at rate ω_0 is qualitatively similar—albeit more involved due to the presence of the second time scale ω_0^{-1} —as discussed in Appendix B.

Consider an initial condition in which N particles are randomly placed on the lattice and each site is given a magnetization at random. The dynamics is such that all sites remain fully ordered at all times, with $m_i = \pm \rho_i$, and the total escape rate is always Nv . A typical trajectory is shown in Fig. 14. It rapidly leads to the emergence of an extensive number of asters, whose rare and sudden evaporations lead to a coarsening dynamics. To characterize the latter, we compute the lifetime of an aster comprising M particles (spread out over the two

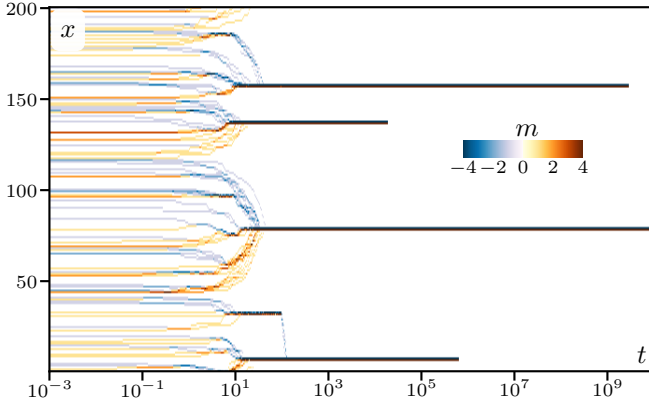


FIG. 14. Starting from a random configuration at $t = 0$ in the zero-temperature model, the system rapidly evolves into a large number of small asters. These coarsen on much longer time scales, as smaller condensates evaporate and are redistributed into larger ones. Parameters: $L = 200$, $N = 100$, $v = 1$, $\varepsilon = 1$.

sites).

Let us consider the situation depicted in Fig. 15 in which an aster is formed with n particles with $+1$ spins at site i and $M - n$ particles with -1 spins at site $i + 1$. We denote this configuration as $\mathbf{n} \equiv (n, M - n)$. The system evolves at rate $q_n = vn$ towards the configuration $\mathbf{n} - \mathbf{1}$ and $p_n = v(M - n)$ towards $\mathbf{n} + \mathbf{1}$. We denote by $r_n = p_n + q_n$ the escape rate from configuration \mathbf{n} , which is here given by $r_n = vM$. Given the expressions of q_n and p_n , there is a linear drift that takes the system towards the most likely configuration $\mathbf{n} = \mathbf{M}/2$. Note that the configurations \mathbf{M} and $\mathbf{0}$ are limiting cases that correspond to the evaporation of the aster. To get an intuitive understanding of the aster dynamics, we consider the master equation of this process:

$$\partial_t P(n) = q_{n+1}P(n+1) + p_{n-1}P(n-1) - (q_n + p_n)P(n). \quad (15)$$

Small Gaussian fluctuations close to the most likely configuration $\mathbf{n} = \mathbf{M}/2$ are well described by introducing $P(x = n/M) = MP(n)$ and expanding (15) to first order in $dx = M^{-1}$. Doing so yields the Fokker-Planck equation

$$\partial_t P(x) = \frac{\partial}{\partial x} \left[V'(x)P(x) + \frac{v}{2M} \frac{\partial}{\partial x} P(x) \right], \quad (16)$$

which corresponds to the dynamics of a Brownian particle in a harmonic potential $V(x) = v(x - \frac{1}{2})^2$ at temperature $\frac{v}{2M}$, as illustrated on Fig. 15. The mean-first passage time τ until the evaporation of an aster with M particles can then be estimated using the Arrhenius scaling $\log \tau \propto M/2$. This scaling is not expected to hold quantitatively, since the diffusive approximation (15) is expected to fail in the large-deviation regime where $x \gg \frac{1}{\sqrt{M}}$, but it captures the physics that makes the aster long-lived at zero temperature.

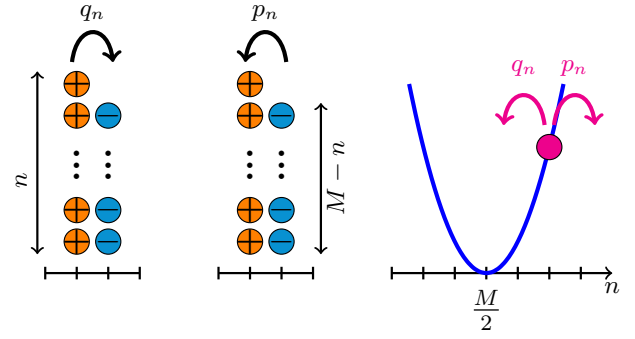


FIG. 15. **Left:** A particle hops out of a site with n particles at a rate $q_n = nv$. This takes the aster from $(n, M - n)$ to $(n - 1, M - n + 1)$. **Center:** A particle hops out of a site with $M - n$ particles at a rate $p_n = (M - n)v$. This takes the aster from $(n, M - n)$ to $(n + 1, M - n - 1)$. **Right:** This dynamics is equivalent to the Brownian dynamics of a single particle at position n , confined in a harmonic potential $V(n) = \frac{v}{2}(\frac{n}{M} - \frac{1}{2})^2$, with $n = 0$ and $n = M$ being absorbing boundaries corresponding to the evaporation of the aster.

We now wish to compute exactly the mean-first passage time to reach either \mathbf{M} or $\mathbf{0}$, which will trigger the redistribution of the aster particles into a neighboring aster, hence driving the coarsening process. Let us note T_n the average evaporation time, starting from configuration \mathbf{n} . In an average time r_n^{-1} , the system jumps to $\mathbf{n} - \mathbf{1}$ or $\mathbf{n} + \mathbf{1}$ with probabilities q_n/r_n and p_n/r_n , respectively. One thus has the recursive relation:

$$T_n = \frac{1}{r_n} + \frac{p_n}{r_n} T_{n+1} + \frac{q_n}{r_n} T_{n-1} \quad (17)$$

that has to be solved with the boundary conditions

$$T_0 = T_M = 0. \quad (18)$$

To do so, we follow standard methods [61, 62] and introduce $U_n = T_{n-1} - T_n$. Equation (17) can then be rewritten as

$$p_n U_{n+1} = q_n U_n + 1. \quad (19)$$

Introducing $\pi_0 = 1$ and, for $i \geq 0$,

$$\pi_i \equiv \prod_{k=1}^i \frac{q_k}{p_k} \quad \text{and, further,} \quad \sigma_i = \sum_{k=1}^i \frac{1}{p_k \pi_k}, \quad (20)$$

Eq. (19) is readily solved as

$$U_{n+1} = \pi_n U_1 + \pi_n \sigma_n. \quad (21)$$

Using $T_0 = 0$, we first get $T_1 = -U_1$. The definition of U_n then recursively leads to

$$T_{n \geq 2} = -U_1 \sum_{i=0}^{n-1} \pi_i - \sum_{i=1}^{n-1} [\pi_i \sigma_i]. \quad (22)$$

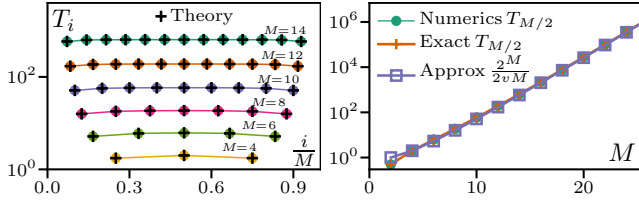


FIG. 16. **Left:** Mean-first-passage times from site i to sites 0 or M , as M varies from 4 to 14. The circles correspond to numerical simulations whereas the crosses correspond to Eq. (24). **Right:** Mean-first passage times to evaporation for an aster with M particles. Green disks are results of numerical simulations, averaged over 10^4 realizations. Orange crosses correspond to the exact formula (24), and purple squares to approximation (30).

Finally, U_1 is determined by imposing the boundary condition $T_M = 0$, which gives:

$$U_1 = -\frac{\sum_{i=1}^{M-1} [\pi_i \sigma_i]}{\sum_{i=0}^{M-1} \pi_i}. \quad (23)$$

All in all, the mean time to evaporation starting from the configuration \mathbf{n} is given by

$$T_n = \frac{\sum_{i=0}^{n-1} \pi_i}{\sum_{i=0}^{M-1} \pi_i} \sum_{i=1}^{M-1} [\pi_i \sigma_i] - \sum_{i=1}^{n-1} [\pi_i \sigma_i] \quad (24)$$

where the second sum vanishes for $n = 1$. The above results are valid for generic random walks with non-vanishing rates p_n and q_n . In the case at hand, using $p_n = v(M - n)$ and $q_n = vn$, we find

$$\pi_i = \binom{M-1}{i}^{-1}, \quad (25)$$

which allows computing T_n .

The mean first passage times to evaporation starting from all possible configurations are plotted in Fig. 16 (left), for M up to 14. Interestingly, T_n becomes rapidly independent of n . This can be understood as follows: due to the asymmetry between p_n and q_n , the most likely path to evaporation is to fall from n to $M/2$ and then to get absorbed. Furthermore, Fig. 16 (left) suggests an exponential increase of T_n with M . To compute the leading order of T_n , consider the various terms of Eq. (24) and their scaling as $M \rightarrow \infty$. We first note, using Eq. (25), that $\pi_0 = \pi_{M-1} = 1$, $\pi_1 = \pi_{M-2} = (M-1)^{-1}$, and $\pi_{1 < i < M-2} = \mathcal{O}(M^{-1})$. Consequently, $\pi_1 + \pi_2 + \dots + \pi_{n-1} \rightarrow 0$ for $n < M$ and only π_0 and π_{M-1} contribute to the sums. Noting also that $(\pi_k p_k)^{-1}$ simplifies into

$$\frac{1}{\pi_k p_k} = \frac{(M-1)!}{vk!(M-k)!} = \frac{1}{vM} \binom{M}{k}, \quad (26)$$

we see that Eq. (24) can be approximated as

$$T_n \sim \frac{1}{2vM} \sum_{i=1}^{M-1} \left[\pi_i \sum_{k=1}^i \binom{M}{k} \right] - \frac{1}{vM} \sum_{i=1}^{n-1} \left[\pi_i \sum_{k=1}^i \binom{M}{k} \right]. \quad (27)$$

Finally, we note that, for $n < M - 1$,

$$\sum_{i=1}^n \left[\pi_i \sum_{k=1}^i \binom{M}{k} \right] < \left[\sum_{i=1}^n \pi_i \right] \left[\sum_{k=1}^{M-2} \binom{M}{k} \right] \quad (28)$$

$$= o \left(\sum_{k=1}^{M-1} \binom{M}{k} \right), \quad (29)$$

so that

$$T_n \sim \frac{1}{2vM} \pi_{M-1} \sum_{k=1}^{M-1} \binom{M}{k} \sim \frac{2^M}{2vM} \quad (30)$$

Figure 16 (right) shows the comparison between numerical measurements of $T_{M/2}$, its exact expression (24) and the asymptotic estimate (30), which is remarkably close to the exact values. The stability of asters and their coarsening at zero temperature thus stems from an evaporation rate that vanishes exponentially with their density.

B. Coarsening at small temperature

At zero temperature, aster coarsening occurs via an extremal dynamics: smallest asters evaporate first and are redistributed among their neighbors. Since the lifetime of an aster diverges exponentially with its height, this leads to an extremely slow dynamics, as apparent from Fig. 14.

At finite temperature, a new phenomenon sets in: when a particle hops forward, as in the second configuration of Fig. 13, it now has a finite probability P_{hop} of hopping further forward and leaving the aster before flipping its spin, with

$$P_{\text{hop}} = \frac{p}{p + W(s \rightarrow -s)}. \quad (31)$$

In an aster comprising two sites with ρ particles, this leads to a flux of particle $j_{\text{leak}}(\rho)$ leaving the aster, where

$$j_{\text{leak}}(\rho) \propto p\rho P_{\text{hop}} = \frac{p^2}{p + W(s \rightarrow -s)} \rho. \quad (32)$$

The variations of $j_{\text{leak}}(\rho)$ with ρ then determine the late-stage dynamics. For the flipping rates (1), $j_{\text{leak}}(\rho) \propto \rho$ at large densities since the hopping rate is bounded, $W(s \rightarrow -s) < \exp(\beta)$: large asters leak particles faster than smaller ones, which arrests the coarsening and lead to a steady-state with an extended number of finite-size asters, as illustrated in Fig. 17a and Fig. 18a-b. (It

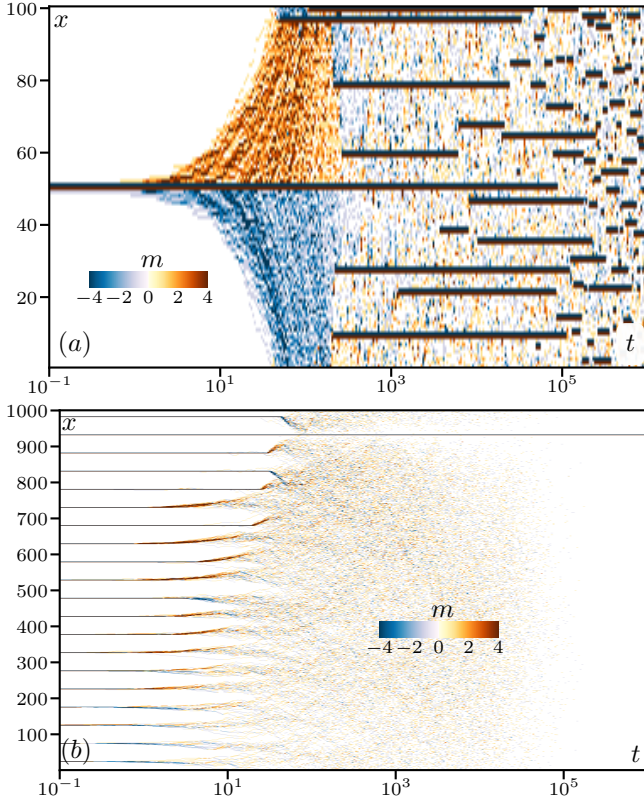


FIG. 17. **(a)** Spatiotemporal plot of the relaxation dynamics from a single aster to the fluctuating aster phase of the AIM with rates (1) ($T = 0.2$, $\varepsilon = 1$, $L = 100$, $\rho_0 = 10$, $D = 0.5$). **(b)**: same as (a) but for the AIM with rates (33), starting from 20 asters whose initial density increases linearly from 6 to 25 as x increases; coarsening leaves a single macroscopic aster ($D = 1$, $L = 1000$, $\omega_0 = 1$, $\beta = 0.375$, $\rho_0 = 0.29$.)

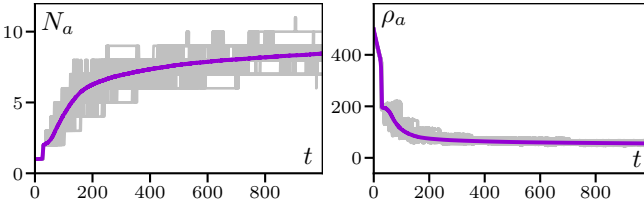


FIG. 18. Relaxation dynamics in the aster phase for the AIM with rates (1). **(a)**: Number of asters as a function of time, averaged over 1000 simulations (magenta). Fifty representative trajectories appear in gray. **(b)**: Same as (a), but for the average density contained in one aster. Parameters as in Fig. 17a.

would be interesting to generalize approaches developed in the past to predict the size of competing finite condensates [63] but this is beyond the scope of this study.) For the unbounded rates studied in [64]:

$$W(s \rightarrow -s) = \omega_0 e^{-\beta s m_i}, \quad (33)$$

larger asters leak slower, leading to a single macroscopic aster, as illustrated in Fig. (17)b. Finally, in a related

1D flocking model, a coarsening into a single structure reminiscent of an aster was observed in the presence of “centering” interactions, which bias the motion of particles towards dense regions [47]. The generality of the mechanisms leading to aster-like structures and their stability is thus an interesting question beyond the sole case of the AIM.

C. Shape of asters

Let us now consider the case $\varepsilon < 1$, where hopping is not fully asymmetric. Thanks to diffusion, particles can hop backward and asters are then spread over several sites. Since they typically comprise many particles, we expect to be able to describe their shape using the mean-field equations (4,5) introduced in Sec. III A. It is straightforward to check that these equations admit stationary solutions of the form

$$\rho(x) = k e^{-\mu_c x}; \quad m(x) = k \phi e^{-\mu_c x} \quad (34)$$

with k a normalization constant and ϕ and μ_c (the subscript “c” stands for “continuous” for a reason that will become apparent shortly) solutions of

$$\frac{v^2}{2D} \phi (\phi^2 - 1) = \phi \cosh(\beta \phi) - \sinh(\beta \phi) \quad (35)$$

$$\mu_c = -v \phi / D. \quad (36)$$

Furthermore, these are the only stationary solutions of Eqs. (4,5) such that $\rho(x)$ and $m(x)$ are proportional to each other. Note that Eq. (34) does not describe the full aster but only half of it, for $x > 0$ or $x < 0$. We are not aware of any analytic solution describing the full aster, including its singularity at $x = 0$. Finally, the competition between the asymmetric hops leading particles towards the aster and the diffusive dynamics allowing them to explore neighboring sites is reminiscent of the diffusive motion of colloids under gravity. The solutions (34) can thus be seen as two exponential atmospheres pointing towards the core of the aster.

We now compare these solutions with the aster profiles measured in the microscopic model in Fig. 19a. The profiles of density and magnetization indeed exhibit an exponential decay on both sides of the aster. In Fig. 19b, we see that the measured decay exponent μ agrees well with the solution μ_c of Eq. (36) at small ε but deviates for larger ε . Note that we plot only the curve $\mu_c(\beta = \infty)$ in Fig. 19b since the curves for different values of β would be indistinguishable on the scale of the figure. Setting $\beta = \infty$ also simplifies the calculation since it amounts to fixing $\phi = \pm 1$ in Eq. (35) so that $\mu_c(\beta = \infty) = \pm v/D = \pm 2\varepsilon$.

Increasing ε , we see that the discrepancy between μ_c and the measured μ increases. This deviation can be attributed to the continuous limit used to derive Eqs. (4,5). If instead we retain the full discrete equations Eqs. (2,3)

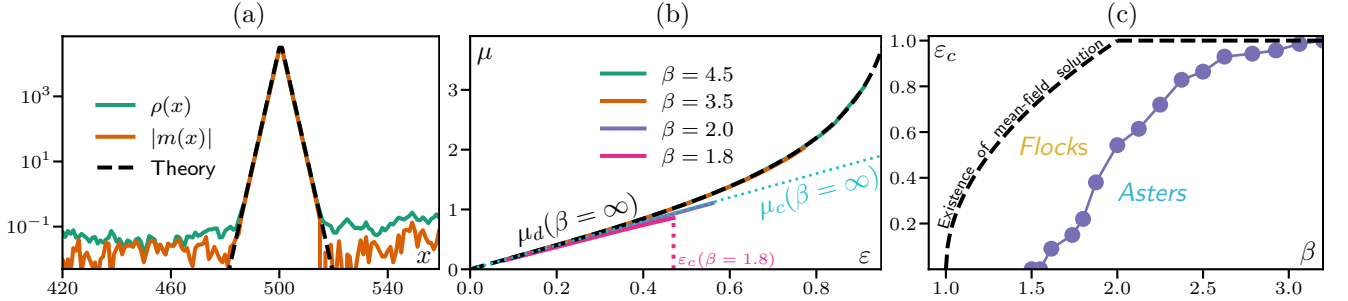


FIG. 19. **(a)**: Profile of an aster in the microscopic model. The dashed lines are the exponential decays predicted by Eqs. (38)-(39). $L = 1000$, $\rho_0 = 100$, $\beta = 4$, $\varepsilon = 0.5$, $D = 0.5$. **(b)**: Measured values of μ in the microscopic model at different β compared with the predictions from the continuous mean-field equations (blue dotted line) and from the discrete ones (black dashed line). $L = 1000$, $\rho_0 = 100$, $D = 0.5$. **(c)**: Phase boundary $\varepsilon_c(\beta)$ such that asters are observed for $\varepsilon < \varepsilon_c$ in microscopic simulations (symbols), compared to the limit of existence of aster solutions in the mean-field equations (dashed line). $L = 500$, $\rho_0 = 10$, $D = 0.5$.

in the mean-field approximation, and look in the same way for exponential solutions

$$\rho_i = k\kappa^i; \quad m_i = k\phi\kappa^i, \quad (37)$$

we find the conditions

$$\frac{4D(\kappa - 1)^2\phi - v(\kappa^2 - 1)}{4\kappa} = \phi \cosh[\beta\phi] - \sinh[\beta\phi] \quad (38)$$

$$\left(\kappa + \frac{1}{\kappa} - 2\right) = \frac{v\phi}{2D}\left(\kappa - \frac{1}{\kappa}\right); \quad \mu_d = -\log \kappa \quad (39)$$

The decay exponent μ_d (where “d” stands for “discrete”) predicted by Eqs. (38,39) is now in near-perfect agreement with microscopic simulations as shown in Fig. 19b.

Interestingly, we find that there is a maximum value of ε that we denote ε_c above which no physical exponential solution is found (we require that $\phi \in [-1, 1]$ and that μ_d be of opposite sign to ϕ for a physical solution). In Fig. 19c, we compare this limit value with the transition line between the flock and aster phases in the microscopic model. Both lines show the same trend as a function of β but are quantitatively different. This indicates that, unsurprisingly, exponential solutions can exist at the mean-field level while asters are not observed because either the full aster solutions do not exist at the mean-field level or because they are unstable to fluctuations.

V. CONCLUSION

We have provided a detailed study of the active Ising model in one space dimension. Despite its simplicity, the AIM shows two non-trivial phases characterized by flocks and asters. We found the flocking phase to exhibit the same properties as in other one-dimensional flocking models [37, 45–50]: Large ordered aggregates spread while propagating, merge when they collide, and regroup when stochastically reversing their direction of motion. As reported before [37, 46, 47], the time between two reversals of a flock increases logarithmically with system

size. We went further and explained this dependence as well as the variations with the velocity of particles and the temperature. In addition, we have also analyzed in detail the flock shapes and how they evolve in time. The global picture is that of a liquid-gas phase separation which cannot relax to steady state because of reversal events. Since this is expected to be generic for 1D flocking models, we thus also expect our analysis of the reversal times based on the flock shapes to be relevant to other systems.

We reported a new phase of the AIM. It is populated by “asters” which are composed of two peaks of opposite magnetization facing each other. These asters appear here only because of the interplay of alignment and self-propulsion and are thus qualitatively different from traffic jams due to steric interactions or from the “dipoles” observed in Ref. [47] which are produced by centering interactions that favor motion towards high-density regions. We have provided an exact solution of the zero-temperature dynamics of an aster and showed that they dissolve in a time that is exponential in their size. At infinite time, this leads to a single aster in the zero-temperature limit but to a finite density of asters at small but finite temperature. Finally, we have shown that asters generically exhibit exponential tails with decay exponents that are well predicted by a mean-field theory.

Common statistical mechanics wisdom states that fluctuations become more important as the dimension of space becomes lower. In equilibrium, this goes as far as preventing the existence of an ordered state in a model with only short-ranged interactions. In our active system, the flocking phase shows that ordering is possible but fluctuations still prevent true symmetry breaking by inducing reversals of the flock direction. Fluctuations play a somewhat different but also essential role in the dynamics of asters: we found that the dissolution of asters and thus their coarsening is due to rare fluctuations, giving rise to extremal dynamics. In contrast, we found that some features of flocks and asters are accounted for to a

good accuracy by a mean-field approach that neglects fluctuations.

ACKNOWLEDGMENTS

We thank Mourtaza Kourbane-Houssene for his early involvement in the project. JT acknowledges financial support from ANR grant THEMA.

Appendix A: Numerical simulations

1. Discrete-time simulations

Our discrete-time simulations are implemented using random sequential updates: Particles are chosen at random and updated sequentially. For each update, the time is increased by dt/N . Denoting by i the site of the chosen particle and by s its spin, the particle either hops, flips its spin, or does nothing with probabilities:

$$\begin{cases} \text{Proba(hop to site } i+1): & D(1+s\varepsilon)dt \\ \text{Proba(hop to site } i-1): & D(1-s\varepsilon)dt \\ \text{Proba(spin flips):} & \omega_0 e^{-\beta s \frac{m_i}{\rho_i}} dt \\ \text{Proba(no update):} & 1 - 2Ddt - \omega_0 e^{-\beta s \frac{m_i}{\rho_i}} dt \end{cases} \quad (\text{A1})$$

In the last case, we say that a move has been “rejected”.

Let us note \mathcal{C}_i the state of particle i , defined by its spin and position. A configuration \mathcal{C} is then given by $\mathcal{C} = \{\mathcal{C}_i\}$. Consider the discrete-time Markov process defined by the above algorithm. Since there is a $1/N$ probability of choosing a given particle, the corresponding discrete-time master equation reads

$$P\left(\mathcal{C}, t + \frac{dt}{N}\right) = \frac{1}{N} \left[\sum_i \sum_{\mathcal{C}'_i \neq \mathcal{C}_i} P(\mathcal{C}', t) W(\mathcal{C}' \rightarrow \mathcal{C}) dt + P(\mathcal{C}, t) \sum_i \left(1 - \sum_{\mathcal{C}'_i \neq \mathcal{C}_i} W(\mathcal{C} \rightarrow \mathcal{C}') dt \right) \right] \quad (\text{A2})$$

where \mathcal{C}' is identical to \mathcal{C} but with particle i in state \mathcal{C}'_i , and the rates W are given by $W = D(1 \pm \varepsilon)$ or by Eq. (1), depending on the transition. It is then straightforward to check that the limit of (A2) as $N \rightarrow \infty$ is the continuous-time master equation of the AIM:

$$\partial_t P(\mathcal{C}, t) = \sum_{\mathcal{C}'_i \neq \mathcal{C}_i} [P(\mathcal{C}', t) W(\mathcal{C}' \rightarrow \mathcal{C}) - P(\mathcal{C}, t) W(\mathcal{C} \rightarrow \mathcal{C}')]]$$

This algorithm has two main limitations. First, it is only exact in the large N limit and it is thus not adapted to study small systems. This precludes using it for the study of the finite-size asters of section IV A. Then, its efficiency relies on the fact that there are as few proposed updates as possible that lead to rejection. Since

the only constraint on the algorithm is that the probabilities in (A1) are between 0 and 1, we take the largest possible dt , given by $dt = (2D + \omega_0 e^\beta)^{-1}$, to minimize the probability of a particle doing nothing during an update.

2. Continuous-time simulations

Our continuous time simulations were implemented as follows. For each particle i , with spin s_i , we define an escape rate $r_i = 2D + \omega_i$, where ω_i is the rate at which s_i flips into $-s_i$. At time 0, we sample a time τ_i for each particle according to $P(\tau_i) = r_i e^{-r_i \tau_i}$. The algorithm then goes iteratively over the following loop:

1. Set the simulation time to $t = \tau_j$ where $\tau_j = \inf_i \tau_i$.
2. Update particle j using tower sampling: pull a random number $\eta \in [0, r_j]$. If $\eta < D(1 - s_j \varepsilon)$, the particle hops to the left. If $D(1 - s_j \varepsilon) < \eta < 2D$, the particle hops to the right. Otherwise, the spin flips: $s_j \rightarrow -s_j$.
3. Update any r_k that has changed because of step 2 and sample new τ_k 's according to $P(\tau_k) = r_k e^{-r_k(\tau_k - t)} \Theta(\tau_k - t)$. A new τ_j is also sampled, whether or not r_j has changed.

To make step 1 as efficient as possible, we use a heap structure, which is a binary sorting tree consisting in a root and two sub heaps. The heap is such that the time stored at a root is always smaller than the times stored at the roots of the two sub heaps. Finding the smallest time then has a cost of $\mathcal{O}(1)$ whereas the reorganization of the heap due to step 3 has a cost $\mathcal{O}(\log_2 N)$.

As we now discuss, the above algorithm, which is a generalization of the celebrated Gillespie algorithm, is an exact implementation of the continuous time Markov chain that defines the AIM. To show that an algorithm simulates a Markov chain defined by transition rates $W(\mathcal{C} \rightarrow \mathcal{C}')$, it suffices to show that trajectories are generated according to two principles. First, the system transitions out of a configuration \mathcal{C} after a time τ distributed as

$$P(\tau) = r(\mathcal{C}) e^{-\tau r(\mathcal{C})} \quad \text{where} \quad r(\mathcal{C}) = \sum_{\mathcal{C}' \neq \mathcal{C}} W(\mathcal{C} \rightarrow \mathcal{C}') \quad (\text{A3})$$

Then, when a configuration change happens, the target configuration \mathcal{C}' is chosen with probability

$$P(\mathcal{C} \rightarrow \mathcal{C}') = \frac{W(\mathcal{C} \rightarrow \mathcal{C}')}{\sum_{\mathcal{C}'' \neq \mathcal{C}} W(\mathcal{C} \rightarrow \mathcal{C}'')} \quad (\text{A4})$$

Consider a case with N possible transitions, with corresponding rates W_i , and take N transition times sampled according to $p(\tau_i) = W_i e^{-W_i \tau_i}$. The probability that the smallest time is larger than τ_{\min} is

$$P(\inf_i \tau_i > \tau_{\min}) = \prod_i \int_{\tau_{\min}}^{\infty} d\tau_i W_i e^{-W_i \tau_i} = e^{-\tau_{\min} \sum_i W_i}$$

so that the probability density of the smallest time $\tau_{\min} = \inf \tau_i$ is given by

$$P(\tau_{\min}) = -\partial_{\tau_{\min}} P(\inf_i \tau_i > \tau_{\min}) = r e^{-\tau_{\min} r},$$

with $r = \sum_i W_i$, which indeed yields Eq. (A3). Tower sampling, as done in step 2, is then a simple way to choose a transition according to (A4).

Note that our algorithm 1-3 relies on two more ingredients. First, for N particles, there are $3N$ possible moves, but we only use N times τ_i , grouping hops and flips to get an escape rate per particle. This is largely arbitrary—and simply appropriate given our data structure—and also leads to the exact implementation of the continuous time Markov chain because the escape rates are linear combinations of the possible rates. Further splitting the transitions into sub-transitions leaves $P(\tau_{\min})$ unchanged since $\sum_i W_i$ remains equal to the total escape rate. Second, we only need to sample new times τ_k at step 3 if r_k has changed, or if the particle k has just moved. This is because the dynamics is Markovian so that any particle n whose time τ_n is larger than t has a waiting time that is already correctly distributed. Indeed, its next configuration change was sampled at an earlier time τ'_n with a law $P(\tau_n) = r_n e^{-r_n(\tau_n - \tau'_n)}$. We now know that τ_n is larger than the current time t , which had a probability $P(\tau_n > t) = e^{-r_n(t - \tau'_n)}$ to happen. Given that τ_n is larger than t , τ_n is thus distributed according to the conditional probability $P(\tau_n)/P(\tau_n > t) = r_n e^{-r_n(\tau_n - t)}$, as it should at time t .

The clear advantages of this continuous-time algorithm are that it is exact and that there is no rejection. At every move, however, several new times τ_k have to be sampled, the heap has to be reorganized, and the data structure is much heavier than for the discrete-time algorithm. As a result, the discrete-time algorithm is always more efficient when the rejection rate is low. For our simulations, the discrete-time simulations were faster at high temperatures, whereas the continuous-time simulations were faster at lower temperature (see Fig. 20) and we used them accordingly.

3. Numerical procedure to spatially align flocks.

We used the rear edge of the flocks to align them. To do so, consider the case of a flock with positive magnetization shown in Fig. 21. We first localize the site i_{\max} where the density is maximal. Going backward from there, i_{back} is the first site where the magnetization changes sign. We then calculate \bar{m} the average magnetization per site over the region of size $2\ell + 1$ centered on i_{\max} , where $\ell \equiv |i_{\max} - i_{\text{back}}|$. Starting from i_{back} , we then find the first site i_{align} such that $m_{i_{\text{align}}} > \bar{m}/4$. All right-going flocks are then aligned such that their site i_{align} coincide. Left-going flocks are transformed by $m_i \rightarrow -m_i$ and $i \rightarrow L - i$ and then run through the same algorithm.

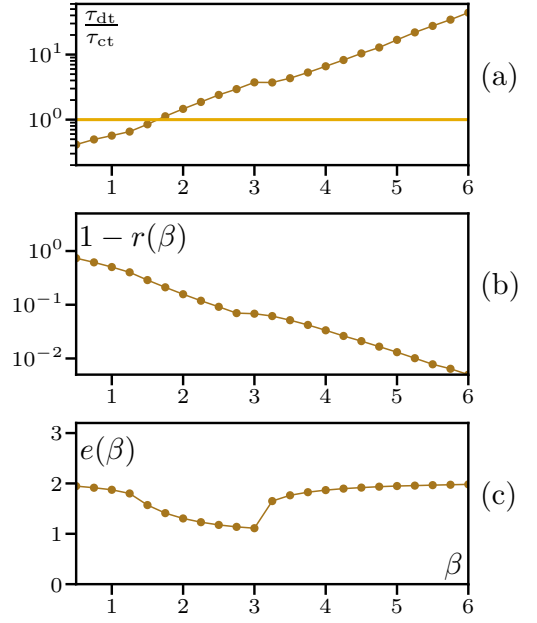


FIG. 20. Comparison between discrete- and continuous-time algorithms. **(a):** Ratio between the cpu time used for a discrete-time simulation, τ_{dt} , and a continuous-time simulations, τ_{ct} , as β is varied. The discrete-time simulation is faster at large temperature but its efficiency decreases exponentially with β . **(b):** The rejection rate of the discrete-time algorithm, $r(\beta)$, converges exponentially to $r(\beta) = 1$ as β increases. **(c):** The average escape rate per particle, $e(\beta)$, shows little variation as β is varied and remains close to $r \simeq 2D + \omega_0$. The dip for intermediate β corresponds to the flocking phase where most particles are aligned. Parameters: $D = 0.5$, $\varepsilon = 1$, $\omega_0 = 1$, $L = 500$, $\rho_0 = 10$. In panel (a), the system is simulated up to a final time $t = 110\,000$.

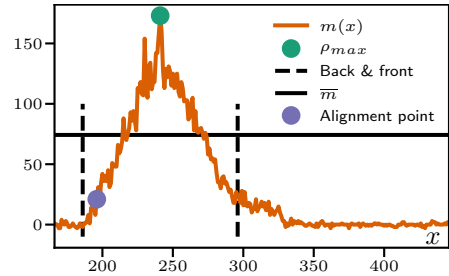


FIG. 21. Sketch of the procedure to align flocks of the same age as described in the text.

Appendix B: Another zero-temperature limit

Considering the AIM at finite temperature and taking the $\beta \rightarrow \infty$ limit lead to a zero-temperature model slightly different from the one treated in Section IV. Indeed, it becomes possible to achieve configurations with vanishing magnetization but finite density. These are such that $n_i^+ = n_i^- \neq 0$, so that their escape rates remain finite as $\beta \rightarrow \infty$ since $W(s \rightarrow -s|m_i = 0) = \omega_0$ for any β . Adding or removing one particle, however, leads

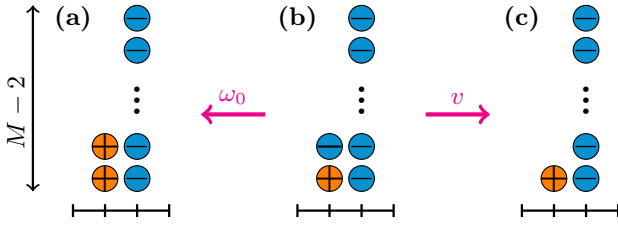


FIG. 22. The zero temperature limit of the AIM admits a new configuration with finite escape rate, shown in (b), where one site can be occupied by two particles with opposite signs, while the second site is occupied by $M - 2$ particles. All moves lead to the evaporation of the aster but two: the minus particle on the first site can flip, at rate ω_0 , to reach the configuration $(2, M - 2)$ depicted in (a); the minus particle on the first site can hop, at rate v , to reach the configuration $(1, M - 2)$ depicted in (c).

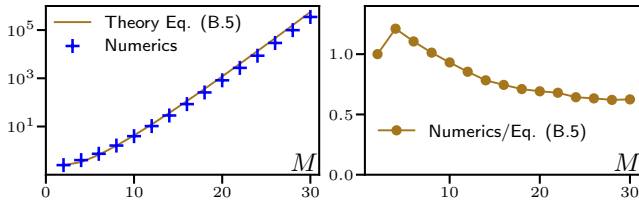


FIG. 23. **Left:** Numerical measurements of the MFPT till evaporation of an aster in the zero-temperature limit of the AIM, compared to the prediction (B5). **Right:** Taking the ratio of the data and the prediction (B5) shows the convergence to a constant slightly different from 1 as $M \rightarrow \infty$, due to the approximation involved in replacing $T_{2,M-2}$ by its former expression (30).

to a non-vanishing magnetization—and hence an immediate spin flip—so that the only new configuration that may play a role is $n_i^+ = n_i^- = 1$.

Let us consider the mean first-passage time starting from an aster with $\frac{M}{2}$ spin + particles at one site and $\frac{M}{2}$ spin - particles at the next site. The dynamics is then identical to that described in Section IV until the aster reaches the configuration $(1, M - 1)$ (or the symmetric case). Then, at rate $v(M - 1)$, it reaches a new configuration, depicted in Fig. 22-b, where the magnetization vanishes on the first site. This leads to the recurrence

$$T_{1,M-1} = \frac{1}{r} + \mathbf{q} T_{d,M-2}, \quad (\text{B1})$$

where $r = vM$ is the total escape rate out of the configuration, $\mathbf{q} = \frac{M-1}{M}$ is the probability that one of the $M - 1$ spin - particles hops forward during the next configuration change, and $T_{d,M-2}$ is the mean first passage time to evaporation starting from the configuration shown in Fig. 22-b. Inspection of the dynamics starting from this configuration then leads to

$$T_{d,M-2} = \frac{1}{r_d} + \frac{v}{r_d} T_{1,M-2} + \frac{\omega_0}{r_d} T_{2,M-2}, \quad (\text{B2})$$

where $r_d = 2\omega_0 + vM$ is the escape rate. Injecting Eq. (B2) into Eq. (B1) then leads to:

$$T_{1,M-1} = \frac{1}{r} + \frac{\mathbf{q}}{r_d} + \frac{\mathbf{q}v}{r_d} T_{1,M-2} + \frac{\mathbf{q}\omega_0}{r_d} T_{2,M-2}. \quad (\text{B3})$$

This has to be compared with the case considered in Section IV, which reads

$$T_{1,M-1} = \frac{1}{r} + \mathbf{q}v T_{2,M-2}. \quad (\text{B4})$$

Two comments are in order. First, Eq. (B3) couples the mean first passage time to evaporation with M and $M - 1$ particles, which makes an exact solution harder to find. Second, in Eq. (B4) $T_{1,M-1} \sim T_{2,M-2}$ as $M \rightarrow \infty$. On the contrary, in Eq. (B3), there is an extra factor $r_d^{-1} \sim 1/M$ between $T_{1,M-1}$ and $T_{2,M-2}$. The new configuration thus makes the evaporation happens M times faster. Since the dynamics close to $M/2$ is insensitive to the details of the dynamics close to the evaporation, it is natural to approximate $T_{2,M-2}$ by its original expression (30). This then leads to the self-consistent scaling

$$T_{1,M-1} \sim \frac{\omega_0}{2\omega_0 + vM} \frac{2^M}{2vM}. \quad (\text{B5})$$

As shown in Fig. 23, scaling (B5) agrees very well with our numerics. The prefactor is, unsurprisingly, incorrect, due to the approximation of $T_{2,M-2}$ by its original expression (30). All in all, the aster still has an average life time that diverges exponentially with its number of particles, and the physics remains qualitatively unaltered from the case discussed in the main text.

- [1] M. C. Marchetti, J. F. Joanny, S. Ramaswamy, T. B. Liverpool, J. Prost, M. Rao, and R. A. Simha, *Reviews of Modern Physics* **85**, 1143 (2013).
- [2] C. Bechinger, R. Di Leonardo, H. Löwen, C. Reichardt, G. Volpe, and G. Volpe, *Reviews of Modern Physics* **88**, 045006 (2016).
- [3] H. Chaté, *Annual Review of Condensed Matter Physics* **11**, 189 (2020).

- [4] J. O'Byrne, Y. Kafri, J. Tailleur, and F. van Wijland, *Nature Reviews Physics*, 1 (2022).
- [5] V. Schaller, C. A. Weber, B. Hammerich, E. Frey, and A. R. Bausch, *Proceedings of the National Academy of Sciences* **108**, 19183 (2011).
- [6] Y. Sumino, K. H. Nagai, Y. Shitaka, D. Tanaka, K. Yoshikawa, H. Chaté, and K. Oiwa, *Nature* **483**, 448 (2012).

- [7] A. Sokolov and I. S. Aranson, Physical review letters **109**, 248109 (2012), publisher: APS.
- [8] H. H. Wensink, J. Dunkel, S. Heidenreich, K. Drescher, R. E. Goldstein, H. Löwen, and J. M. Yeomans, Proceedings of the National Academy of Sciences **109**, 14308 (2012).
- [9] H. M. López, J. Gachelin, C. Douarche, H. Auradou, and E. Clément, Physical review letters **115**, 028301 (2015).
- [10] G. Liu, A. Patch, F. Bahar, D. Yllanes, R. D. Welch, M. C. Marchetti, S. Thutupalli, and J. W. Shaevitz, Physical review letters **122**, 248102 (2019), publisher: APS.
- [11] A. Curatolo, N. Zhou, Y. Zhao, C. Liu, A. Daerr, J. Tailleur, and J. Huang, Nature Physics **16**, 1152 (2020).
- [12] A. Cavagna, A. Cimorelli, I. Giardina, G. Parisi, R. Santagati, F. Stefanini, and M. Viale, Proceedings of the National Academy of Sciences **107**, 11865 (2010).
- [13] J. Gautrais, F. Ginelli, R. Fournier, S. Blanco, M. Soria, H. Chaté, and G. Theraulaz, Plos computational biology **8**, e1002678 (2012).
- [14] A. Attanasi, A. Cavagna, L. Del Castello, I. Giardina, S. Melillo, L. Parisi, O. Pohl, B. Rossaro, E. Shen, E. Silvestri, et al., PLoS computational biology **10**, e1003697 (2014).
- [15] W. Poel, B. C. Daniels, M. M. Sosna, C. R. Twomey, S. P. Leblanc, I. D. Couzin, and P. Romanczuk, Science Advances **8**, eabm6385 (2022), publisher: American Association for the Advancement of Science.
- [16] J. R. Howse, R. A. Jones, A. J. Ryan, T. Gough, R. Vafabakhsh, and R. Golestanian, Physical review letters **99**, 048102 (2007).
- [17] I. S. Aranson, Physics-Uspekhi **56**, 79 (2013), publisher: IOP Publishing.
- [18] J. Zhang, B. A. Grzybowski, and S. Granick, Langmuir **33**, 6964 (2017), publisher: ACS Publications.
- [19] F. Ginot, A. Solon, Y. Kafri, C. Ybert, J. Tailleur, and C. Cottin-Bizonne, New Journal of Physics **20**, 115001 (2018).
- [20] A. Bricard, J.-B. Caussin, N. Desreumaux, O. Dauchot, and D. Bartolo, Nature **503**, 95 (2013).
- [21] D. Geyer, D. Martin, J. Tailleur, and D. Bartolo, Physical Review X **9**, 031043 (2019), publisher: APS.
- [22] H. Karani, G. E. Pradillo, and P. M. Vlahovska, Physical review letters **123**, 208002 (2019), publisher: APS.
- [23] Z. T. Liu, Y. Shi, Y. Zhao, H. Chaté, X.-q. Shi, and T. H. Zhang, Proceedings of the National Academy of Sciences **118**, e2104724118 (2021), publisher: National Acad Sciences.
- [24] J. Deseigne, O. Dauchot, and H. Chaté, Physical Review Letters **105**, 098001 (2010).
- [25] N. Kumar, H. Soni, S. Ramaswamy, and A. Sood, Nature communications **5**, 1 (2014), publisher: Nature Publishing Group.
- [26] H. Soni, N. Kumar, J. Nambisan, R. K. Gupta, A. Sood, and S. Ramaswamy, Soft Matter **16**, 7210 (2020), publisher: Royal Society of Chemistry.
- [27] T. Vicsek, A. Czirók, E. Ben-Jacob, I. Cohen, and O. Shochet, Physical review letters **75**, 1226 (1995).
- [28] J. Toner and Y. Tu, Physical Review Letters **75**, 4326 (1995).
- [29] N. D. Mermin and H. Wagner, Physical Review Letters **17**, 1133 (1966).
- [30] S. Ramaswamy, R. A. Simha, and J. Toner, EPL (Euro-physics Letters) **62**, 196 (2003).
- [31] H. Chaté, F. Ginelli, G. Grégoire, and F. Raynaud, Physical Review E **77**, 046113 (2008).
- [32] S. Dey, D. Das, and R. Rajesh, Physical review letters **108**, 238001 (2012).
- [33] B. Mahault, F. Ginelli, and H. Chaté, Physical Review Letters **123**, 218001 (2019), publisher: APS.
- [34] F. Ginelli and H. Chaté, Physical Review Letters **105**, 168103 (2010).
- [35] Y.-L. Chou, R. Wolfe, and T. Ihle, Physical Review E **86**, 021120 (2012).
- [36] A. Peshkov, S. Ngo, E. Bertin, H. Chaté, and F. Ginelli, Physical Review Letters **109**, 098101 (2012).
- [37] A. Solon and J. Tailleur, Physical review letters **111**, 078101 (2013).
- [38] D. Martin, H. Chaté, C. Nardini, A. Solon, J. Tailleur, and F. Van Wijland, arXiv preprint arXiv:2008.01397 (2020).
- [39] G. Grégoire and H. Chaté, Physical review letters **92**, 025702 (2004).
- [40] A. P. Solon, H. Chaté, and J. Tailleur, Physical review letters **114**, 068101 (2015).
- [41] L. Van Hove, Physica **16**, 137 (1950), publisher: Elsevier.
- [42] C. Domb, R. K. Zia, B. Schmittmann, and J. L. Lebowitz, Statistical mechanics of driven diffusive systems, Vol. 17 (Academic Press, 1995).
- [43] M. Evans, Y. Kafri, H. Koduvely, and D. Mukamel, Physical review letters **80**, 425 (1998).
- [44] Y. Kafri, E. Levine, D. Mukamel, G. M. Schütz, and J. Török, Physical review letters **89**, 035702 (2002).
- [45] A. Czirók, A.-L. Barabási, and T. Vicsek, Physical Review Letters **82**, 209 (1999).
- [46] O. J. O’Loan and M. R. Evans, Journal of Physics A: Mathematical and General **32**, L99 (1999).
- [47] J. Raymond and M. Evans, Physical Review E **73**, 036112 (2006), publisher: APS.
- [48] V. Dosssetti, Journal of Physics A: Mathematical and Theoretical **45**, 035003 (2011), publisher: IOP Publishing.
- [49] E. O. Laighléis, M. R. Evans, and R. A. Blythe, Physical Review E **98**, 062127 (2018), publisher: APS.
- [50] H. Sakaguchi and K. Ishibashi, Physical Review E **100**, 052113 (2019), publisher: APS.
- [51] J. Buhl, D. J. Sumpter, I. D. Couzin, J. J. Hale, E. Despland, E. R. Miller, and S. J. Simpson, Science **312**, 1402 (2006).
- [52] C. A. Yates, R. Erban, C. Escudero, I. D. Couzin, J. Buhl, I. G. Kevrekidis, P. K. Maini, and D. J. Sumpter, Proceedings of the National Academy of Sciences **106**, 5464 (2009), publisher: National Acad Sciences.
- [53] T. Bertrand, J. d’Alessandro, A. Maitra, S. Jain, B. Mercier, R.-M. Mège, B. Ladoux, and R. Voituriez, arXiv preprint arXiv:2012.00785 (2020).
- [54] A. P. Solon and J. Tailleur, Physical Review E **92**, 042119 (2015), publisher: APS.
- [55] In this limit, the hopping dynamics can be seen as an equilibrium dynamics at infinite temperature, while the flipping dynamics occurs at temperature T .
- [56] K. Binder and D. Landau, Physical Review B **30**, 1477 (1984).
- [57] A. P. Solon, J.-B. Caussin, D. Bartolo, H. Chaté, and J. Tailleur, Physical Review E **92**, 062111 (2015).

- [58] In practice we choose as a criterion that the fluctuation has propagated if the magnetization at a distance $L = 30$ sites from the initial fluctuation has changed sign.
- [59] K. Kruse, J.-F. Joanny, F. Jülicher, J. Prost, and K. Sekimoto, Physical review letters **92**, 078101 (2004).
- [60] F. Farrell, M. Marchetti, D. Marenduzzo, and J. Tailleur, Physical review letters **108**, 248101 (2012).
- [61] N. G. Van Kampen, Stochastic processes in physics and chemistry, Vol. 1 (Elsevier, 1992).
- [62] T. Antal and I. Scheuring, Bulletin of mathematical biology **68**, 1923 (2006).
- [63] A. G. Thompson, J. Tailleur, M. E. Cates, and R. A. Blythe, Journal of Statistical Mechanics: Theory and Experiment **2010**, P02013 (2010).
- [64] M. Kourbane-Houssene, C. Erignoux, T. Bodineau, and J. Tailleur, Physical review letters **120**, 268003 (2018).